






Magnetic transition and spin-polarized two-dimensional electron gas controlled by polarization switching in strained $\text{CaMnO}_3/\text{BaTiO}_3$ slabs

S. Di Napoli ^{1,2}, A. Román ^{1,3}, A. M. Llois ^{1,2}, M. H. Aguirre ^{4,5,6}, L. B. Steren ^{1,3} and M. A. Barral^{1,2}

¹*Instituto de Nanociencia y Nanotecnología CNEA - CONICET, Nodo Constituyentes, Av. Gral. Paz 1499, B1650KNA San Martín, Prov. Buenos Aires, Argentina*

²*Departamento de Física de la Materia Condensada, GIyA-CNEA, Av. Gral. Paz 1499, B1650KNA San Martín, Prov. Buenos Aires, Argentina*

³*Laboratorio de Nanoestructuras Magnéticas y Dispositivos, Centro Atómico Constituyentes, Av. Gral. Paz 1499, B1650KNA San Martín, Prov. Buenos Aires, Argentina*

⁴*Instituto de Nanociencia y Materiales de Aragón, CSIC, E-50018 Zaragoza, Spain*

⁵*Departamento de Física de la Materia Condensada, Universidad de Zaragoza, E-50009 Zaragoza, Spain*

⁶*Laboratorio de Microscopías Avanzadas, Universidad de Zaragoza, E-50018 Zaragoza, Spain*



(Received 21 December 2023; revised 19 February 2024; accepted 22 February 2024; published 27 March 2024)

Ab initio calculations show the presence of a strong magnetoelectric interfacial coupling in a CaMnO_3 ultrathin film grown on a strained BaTiO_3 ferroelectric film. This heterostructure presents a polarization driven magnetic transition from a G-type to an A-type antiferromagnetic structure. Together with this magnetic transition we find a metallic behavior at the interface between these two insulators, where the charge character of the carriers can be tuned from electrons to holes by switching the electric polarization direction of the ferroelectric film. Besides, the electron gas is spin polarized while the hole gas is not.

DOI: [10.1103/PhysRevMaterials.8.034408](https://doi.org/10.1103/PhysRevMaterials.8.034408)

I. INTRODUCTION

During the last decades, a lot of effort has been made to design heterostructures consisting of a ferroelectric (FE) and a magnetic material, with a large interfacial magnetoelectric coupling, in order to be technologically used to control magnetism through electric fields [1–3]. In the quest for functional materials, perovskites have emerged as prominent candidates due to their robust coupling among structural, orbital, charge, and spin degrees of freedom. With remarkable advancements in thin film growth techniques for perovskite oxides, precise atomic control over surfaces and interfaces has been achieved, amplifying the appeal of this material class for applications in energy, information storage, and spintronics.

Antiferromagnetic materials produce no demagnetization fields, are robust against magnetic field perturbations, and show ultrafast dynamics with large magnetotransport responses [4]. Therefore, particular attention should be given to antiferromagnetic manganites within magnetic perovskites. Additionally, in manganites, the exchange interactions can be regarded as a competition between ferromagnetic double-exchange (DE) [5,6] and antiferromagnetic superexchange interactions (SE) [7,8]. Consequently, the magnetic interaction among Mn ions is highly sensitive to lattice distortions and the local electronic and chemical environment, resulting in a diverse array of magnetic structures.

It is also technologically important and by now already well established that when putting together certain insulating oxides, high mobility carriers, i.e., a two-dimensional electron gas (2DEG), can emerge as a consequence of the interfacial electronic reconstruction. The most widely studied

2DEG is the one originated at SrTiO_3 (001) surface [9] and interfaces, such as $\text{LaAlO}_3/\text{SrTiO}_3$ (LAO/STO) [10–13] and $\gamma\text{-Al}_2\text{O}_3/\text{STO}$ [14]. In almost all the cases, the electronic reconstruction is a consequence of either the presence of oxygen vacancies at the surface or is due to the polar discontinuity at interfaces [15]. But there might be other mechanisms yielding to the formation of a 2DEG, like the discontinuity of the charge ordering that takes place at the (001) surface of the Peierls-like semiconductor BaBiO_3 [16], or at the $\text{BaBiO}_3/\text{BaPbO}_3$ interface [17,18]. Furthermore, in the last few years a lot of work has been done in order to control the interfacial electronic reconstruction with the concomitant generation of the 2DEG [19,20]. For instance, it was recently predicted that a 2DEG developed at the polar/nonpolar $\text{LaInO}_3/\text{BaSnO}_3$ interface or at the ferroelectric/nonpolar $\text{PbTiO}_3/\text{SrTiO}_3$ interface can be tuned [21–23].

In a previous work, we have analyzed the effect of high tensile strain and low dimensionality on the magnetic and electronic properties of CaMnO_3 (CMO) ultrathin films epitaxially grown on SrTiO_3 (STO) substrates, both, computationally and experimentally [24]. From the computational simulations, we have found that the combination of both effects yields a change in the magnetic order of CaMnO_3 ultrathin films, from the G-type antiferromagnetic (GAF) structure present in the bulk compound to an A-type antiferromagnetic (AAF) one. This magnetic change is also coupled to an insulator-metal transition.

In the present work, we explore if the magnetic and the insulator-metal transitions, together with the concomitant generation of a 2DEG, can be triggered and controlled by reversing the electric polarization of a ferroelectric layer in

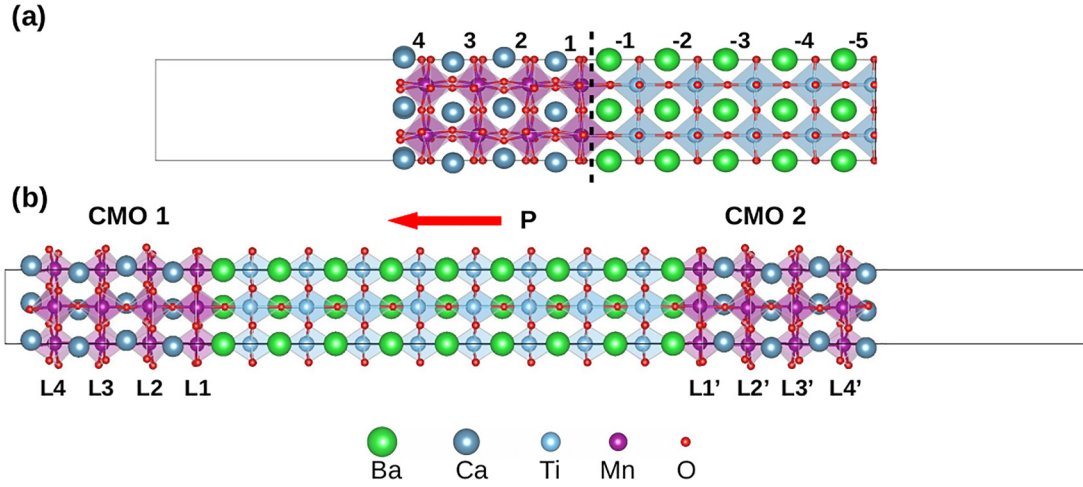


FIG. 1. (a) Unit cell of $(\text{CaMnO}_3)_4/(\text{BaTiO}_3)_5$ heterostructure. In this sketch, the polarization is pointing to the CMO film ($\mathbf{P} \uparrow$). (b) $\text{CaMnO}_3/4/(\text{BaTiO}_3)_{8.5}/(\text{CaMnO}_3)_4$ trilayer. The figures were generated using the VESTA software package [49].

contact with the CaMnO_3 ultrathin film, yielding to an interfacial magnetoelectric coupling (IMEC) characterized by a magnetic reconstruction. Our goal is twofold: on one hand, the pursued IMEC effect would be different and larger than the usual one [25–27] since the change in the magnetization would be due to a change in the magnetic coupling between the Mn’s moments of the ultrathin CMO film instead of coming from a variation in the magnitude of local magnetic moments [28,29]. On the other hand, the tunable 2DEG could be spin polarized due to the magnetic nature of the heterostructure.

The ferroelectric material under consideration is the tetragonal BaTiO_3 (BTO), which shows an electric remanent polarization in the (001) direction [30]. It is worth mentioning that we choose these materials motivated by the experimental findings that show the possibility of epitaxial growth of high quality BaTiO_3 and CaMnO_3 ultrathin films on SrTiO_3 substrates. In our previous work, we show that CMO can be coherently grown on a (001)- SrTiO_3 substrate, presenting a sharp interface with negligible atomic disorder [24]. Images of epitaxial BTO/STO taken by high resolution scanning transmission electron microscopy with high angular annular dark field detector (HRSTEM-HAADF) can be found in the Supplemental Material of the present work [31].

II. COMPUTATIONAL DETAILS

We perform first-principles calculations within the framework of density functional theory and the projector augmented wave (PAW) method [32], as implemented in the Vienna *ab initio* simulation package (VASP) [33,34]. We explicitly treat 10 valence electrons for Ca ($3s^2 3p^6 4s^2$), 13 for Mn ($3p^6 3d^5 4s^2$), 10 for Ba ($5s^2 5p^6 6s^2$), 12 for Ti ($3s^2 3p^6 3d^2 4s^2$), and 6 for O ($2s^2 2p^4$). The local spin density approximation (LSDA) in the parametrization of Ceperley and Alder is used [35,36]. As is already shown, for manganese perovskites this approximation successfully predicts the observed stable magnetic phase and the structural parameters [37–39]. Moreover, for BaTiO_3 , the ferroelectric lattice distortion, spontaneous polarization, and lattice dynamics predicted by LSDA agree

well with experimental results [40–42]. We include a Hubbard term with $U = 5$ eV and $J = 1$ eV within the Lichtenstein implementation [43] for a better treatment of the Mn $3d$ electrons in CaMnO_3 . We have checked the robustness of our results with respect to the U and J parameters, finding that the stable magnetic structure of bulk Pnma CaMnO_3 corresponds to a G-type antiferromagnetic configuration, in agreement with experimental results. Moreover, the used parameters lead to a band gap of 1.60 eV, close to the experimental value of 1.55 eV [44].

The $\text{CaMnO}_3/\text{BaTiO}_3$ grown on SrTiO_3 slabs are modeled by a 2×2 in-plane supercell of the pseudocubic perovskite structure, with a five unit cells thick layer (~ 1.8 nm) of BaTiO_3 and a four unit cells thick layer of CaMnO_3 . The MnO_2 termination of CMO in contact with the BaTiO_3 layer and the CaO termination facing the vacuum region, are considered, as depicted in Fig. 1(a). The SrTiO_3 substrate is not explicitly treated, but is implicitly included by constraining the in-plane lattice constant of the whole structure to the optimized bulk cell parameter of STO ($a_{\text{STO}} = 3.87$ Å). The considered BTO thickness was demonstrated to be sufficient for the ferroelectric instability to develop. [25,45–47] At the same time, it is thin enough to be fully strained when grown on the substrate (see the SM).

We relax the internal coordinates of all atoms within the CMO film and the two BTO layers adjacent to the CMO. The remaining atoms in the BTO film are fixed at their bulklike and previously optimized positions in the strained bulk calculations, in order to fix its ferroelectric polarization, which was determined from first principles using the Berry-phase formalism [48]. A vacuum spacer of 17.5 Å along the z axis was used in order to avoid the self-interaction through the periodic boundary conditions. In addition, since the BTO layer has a net dipole moment oriented along the (001) direction, the dipole correction, as implemented in VASP, was used. We call the ferroelectric polarization \mathbf{P} “up” ($\mathbf{P} \uparrow$) when it is pointing to the interface and “down” ($\mathbf{P} \downarrow$) when it is pointing away from the CMO/BTO interface.

Similar to our previous work [24], we consider the most relevant antiferromagnetic (AF) orders that might be shown

by the Mn atoms, namely AAF (ferromagnetic (FM) ordered (001) planes that align antiparallel with neighboring planes along the [001] direction), CAF [AF alignment within the (001) planes and FM between adjacent planes] and GAF (AF coupling between first nearest neighbors). It is worth mentioning that the noncollinearity of the Mn magnetic structure is known to be quite minimal and gives rise to a small magnetic moment of $0.04\mu_B$ [50,51], and therefore we approximate the magnetic configuration with a collinear model.

All the DFT calculations are performed using a 500 eV energy cutoff in the plane waves basis. We use a $6 \times 6 \times 1$ Monkhorst-Pack k -point grid centered at the Γ point to evaluate integrals within the Brillouin zone (BZ). The structural relaxations are performed until the forces on each ion are less than 0.01 eV/Å.

We also address the electronic and magnetic properties of the interface between strained CaMnO_3 and BaTiO_3 using an alternative structural model consisting of a $(\text{CaMnO}_3)_4/(\text{BaTiO}_3)_{8.5}/(\text{CaMnO}_3)_4$ (CMO1/BTO/CMO2) trilayer. The nonstoichiometry of the BTO film is necessary in order to obtain the BaO termination of both interfaces. The in plane unit cell is a $\sqrt{2} \times \sqrt{2}$ supercell of the pseudocubic perovskite structure containing two transition metals (Mn/Ti) per plane and a vacuum spacer along the z axis of 18.8 Å, as depicted in Fig. 1(b). All the computation parameters (plane wave's energy cutoff, k -points grid, ionic relaxation, and dipole correction) are set to guarantee the convergence of our results. Within this structural model, the CMO1/BTO interface represents the previous $P \uparrow$ regime while the BTO/CMO2 corresponds to the $P \downarrow$ one and, therefore, we can simulate both polarization regimes simultaneously.

III. RESULTS AND DISCUSSION

As was already known for more than three decades, bulk crystalline BTO shows a cubic symmetry and is paraelectric above $T_c = 393$ K, becomes tetragonal and ferroelectric below T_c , and goes through additional transitions to orthorhombic at 278 K and rhombohedral at 183 K. [52] In its tetragonal phase, BaTiO_3 shows an electric remanent polarization $P_{\text{BTO}} \simeq 26 \mu\text{C}/\text{cm}^2$ in the (001) direction [30].

As a first step, we calculate the polarization value of tetragonal BaTiO_3 when it is epitaxially grown on top of a cubic (001) SrTiO_3 substrate, whose lattice constant was previously optimized within the LDA. Under compressive epitaxial strain, its polarization increases with increasing tetragonality and was predicted to be enhanced for large compressive misfit, as the one imposed by a coherent epitaxial growth on perovskite substrates having a smaller lattice constant, such as SrTiO_3 [40]. Under this compressive misfit strain of $\simeq -2.2\%$ imposed by the substrate, the spontaneous polarization is enhanced by 34% ($P_{\text{BTO/STO}} = 37.4 \mu\text{C}/\text{cm}^2$) compared to its value in the unconstrained bulk tetragonal phase ($P_{\text{BTO}} = 27.9 \mu\text{C}/\text{cm}^2$). In Table I we show the computed P values for different in-plane (a) parameters, corresponding to the experimental value, the LDA relaxed BaTiO_3 and SrTiO_3 in-plane lattice constants. In all the cases, the out-of-plane (c) lattice parameters were optimized. As expected, we find an enhancement of the ferroelectric polarization due to the

TABLE I. BTO polarization values along the (001) direction, calculated for different in-plane (a) and out-of-plane (c) lattice parameters.

	a (Å)	c (Å)	P_z ($\mu\text{C}/\text{cm}^2$)
Experimental BTO [52]	3.991	4.035	26.0
Bulk BTO	3.942	4.004	27.9
Strained bulk BTO	3.867	4.100	37.4

compressive strain, with the corresponding elongation of the c parameter, in agreement with previous reported calculations [40,41].

To study the influence of the FE polarization switching in the magnetic properties of the CMO film, we consider a $(\text{CaMnO}_3)_4/(\text{BaTiO}_3)_5$ bilayer, such as the one depicted in Fig. 1(a). We take into account three polarization regimes, that is $P \uparrow$, $P \downarrow$, and $P = 0$, where the last one corresponds to the centrosymmetric structure of BaTiO_3 . In Table II, the total energies referred to the GAF-magnetic structure within each P regime are informed. As it can be seen, the GAF type is the most stable magnetic structure for $P = 0$ and $P \downarrow$ polarizations, while the AAF type is the ground state in the case of $P \uparrow$.

To understand the origin of this ferroelectric-driven magnetic transition, we analyze the layer-resolved partial density of states (PDOS) for the ground states of the $P \uparrow$ and $P \downarrow$ regimes and compare them to the $P = 0$ case (see Figs. 2–4). For the nonpolarized centrosymmetric BTO structure, we find that the whole heterostructure remains insulating. It is interesting to note for our future analysis that, due to the tensile strain in the CMO film, the degeneracy of the two empty Mn's e_g orbitals is lifted and the bottom of the conduction band has a $d_{x^2-y^2}$ character, as can be seen in the left panel of Fig. 2.

When the polarization points to the CMO film, an electronic reconstruction emerges in order to screen the positive polarization charge, as shown in the left upper panel of Fig. 3. It can be seen from this figure that charge transferred from the BTO to the CMO film begins to fill the empty Mn- d conduction bands and this effect continues through all four CMO layers. Due to the broken degeneracy of the e_g orbitals, the ones which begin to be partially occupied are the $d_{x^2-y^2}$ ones. As known, the magnetic interaction between the Mn atoms is determined by the competition between AFM superexchange via the Mn t_{2g} electrons and FM double exchange via the Mn e_g electrons. When the $d_{x^2-y^2}$ orbitals are partially

TABLE II. Energy with respect to the corresponding GAF-magnetic configuration (in meV/f.u.) for the different orientations of the BaTiO_3 polarization in the $(\text{CMO})_4/(\text{BTO})_5$ heterostructure. The energies corresponding to zero polarization is also shown, for comparison.

Mag.Conf.	$P \uparrow$	$P \downarrow$	$P = 0$
GAF	0.0	0.0	0.0
AAF	-18.0	8.3	10.7
CAF	11.6	9.8	12.1
FM	-0.9	22.4	27.5

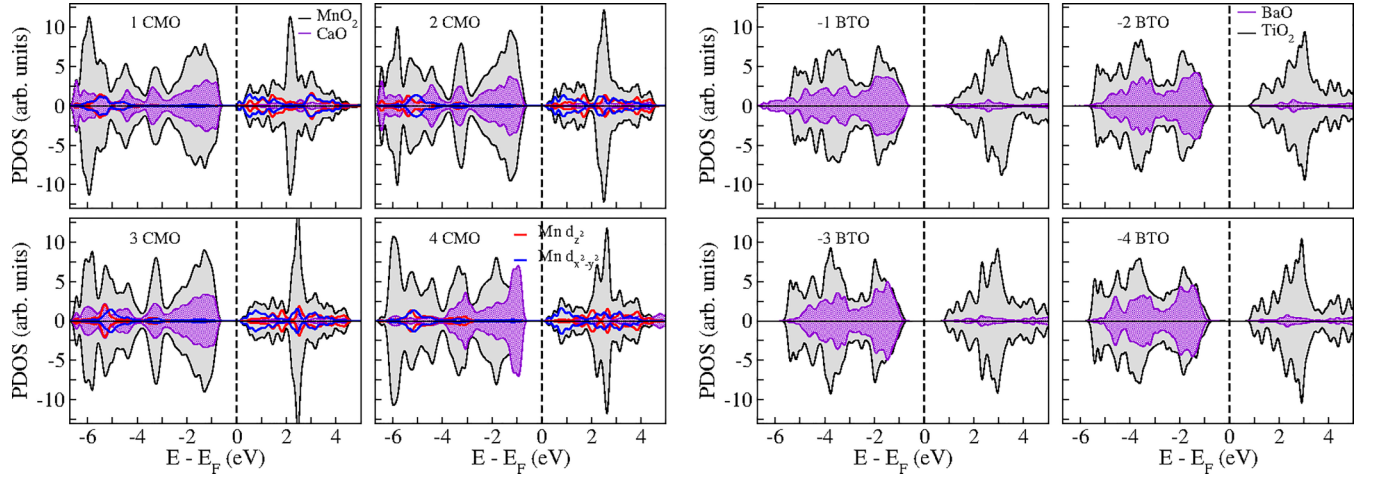


FIG. 2. Layer resolved PDOS of CMO (left) and BTO (right) layers (excluding the BTO-vacuum interface), corresponding to $P=0$. In blue (red) the Mn $d_{x^2-y^2}$ (d_{z^2}) character is shown.

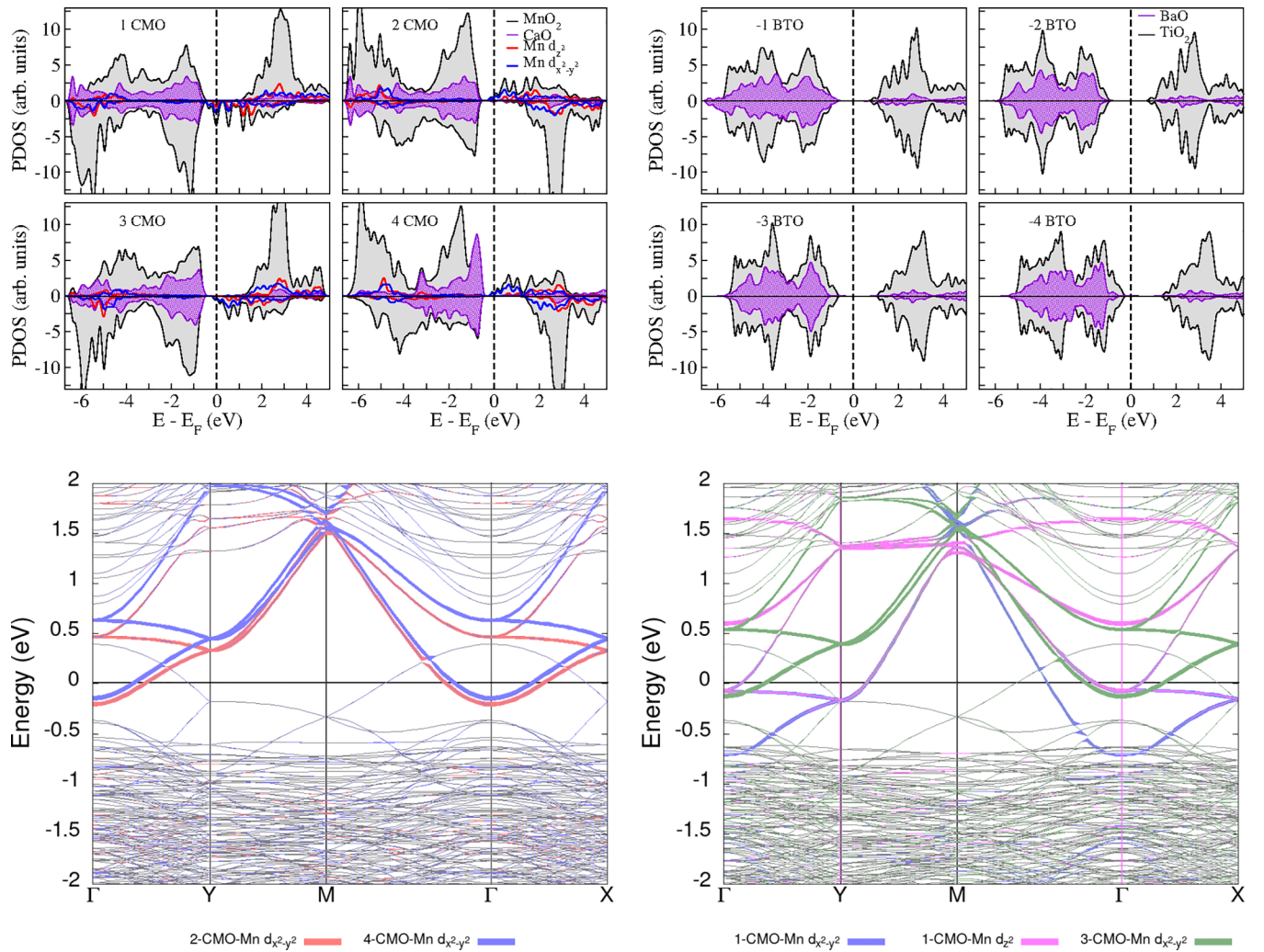


FIG. 3. Upper panels: layer resolved PDOS of CMO (left) and BTO (right) layers (excluding the BTO-vacuum interface) for the case of polarization pointing to the CMO interface ($P \uparrow$). Lower panels: spin up (left) and spin down (right) bandstructure of the heterostructure. The different character of the Mn's e_g orbitals coming from each CMO layer is highlighted.

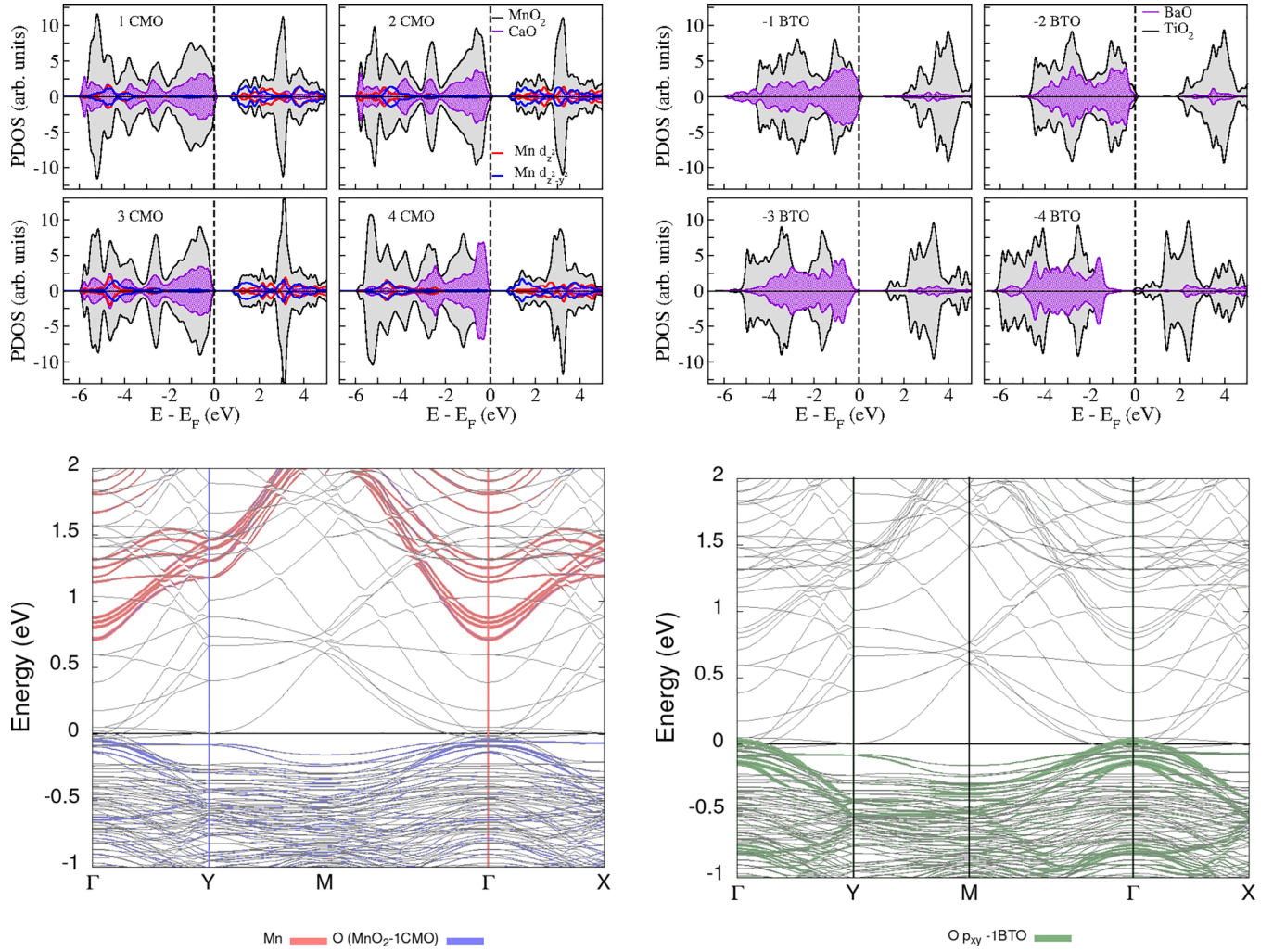


FIG. 4. Upper panels: layer resolved PDOS of CMO (left) and BTO (right) layers (excluding the BTO-vacuum interface) for the case of polarization pointing away from the CMO interface ($P \downarrow$). Lower panels: spin (up+down) bandstructure of the heterostructure. Projections onto the Mn- e_g and interfacial O(CMO) orbitals (left) and onto interfacial O $p_x + p_y$ (BTO) (right) are highlighted. Ti bands are above 2.5 eV.

occupied, the double exchange in the MnO_2 planes strengthens the FM ordering while superexchange stabilizes the AFM one between the planes, leading to the AAF magnetic ground state. Coupled to this polarization driven magnetic transition, we find an insulator to metal transition characterized by an extended two dimensional electron gas (2DEG) which is mainly localized at the interface. A rough estimation of this charge transfer can be calculated from the computed polarization value of $37.4 \mu\text{C}/\text{cm}^2$, which gives a net charge of around $1.4 e^-$ when taking into account our surface unit cell. This value is consistent with the one obtained when integrating the density of states corresponding to the CMO conduction bands, namely $\simeq 1.03 e^-$, which is the charge inside the atomic spheres given by the used pseudopotentials. This charge is spin polarized, with a net magnetic moment of $0.2 \mu_B$, due to the uncompensated magnetic moments between the CMO layers (see Table III). This feature can also be observed in the bottom panels of Fig. 3, where we show the spin up (left) and spin down (right) bandstructure projected onto the Mn- $d_{x^2-y^2}$ bands of all the layers. For the interfacial Mn atoms we also plot the d_{z^2} character of the bands, which are slightly occupied. It can be noted that the spin-down Mn- $d_{x^2-y^2}$ band

corresponding to the interfacial 1-CMO layer is shifted with respect to the spin-up Mn $d_{x^2-y^2}$ of the 2-CMO one, which gives rise to the uncompensated magnetic moment of the whole CMO film. As expected, the electronic reconstruction induced by the FE polarization decreases when going far from the interface. The interfacial band that crosses the Fermi level (highlighted in blue in the right bottom panel of Fig. 3) presents a slightly anisotropic dispersion around the Γ point with estimated effective masses of $0.48 m_e$ and $0.37 m_e$, for the Γ -X and the Γ -M directions, respectively. These values are of the same order as the ones reported for the 2DEG generated at the $\text{SrTiO}_3/\text{LaAlO}_3$ interfaces [15].

TABLE III. Mn magnetic moments (in μ_B) within each MnO_2 layer, from one to four, as labeled in Fig. 1(a).

		1	2	3	4
$P = 0$	GAF	± 2.74	∓ 2.78	± 2.78	∓ 2.79
$P \uparrow$	AAF	-3.05	2.85	-2.85	2.85
$P \downarrow$	GAF	± 2.74	∓ 2.78	± 2.78	∓ 2.79

TABLE IV. Energy with respect to the equilibrium magnetic configuration, ΔE , in meV/f.u., for both CMO1 and CMO2 layers [see Fig. 1(b)].

CMO1-CMO2 magnetic configuration	ΔE
AAF - AAF	4.4
AAF - GAF	0.0
GAF - AAF	13.1
GAF - GAF	9.4

When the polarization is pointing away from the CMO-film ($P \downarrow$) we find a slight electron's depletion at the first two layers of the BTO film (i.e., -1 BTO and -2 BTO), which gives rise to a two dimensional hole gas (2DHG) located within these two layers (see upper panels of Fig. 4). For this polarization direction, the CMO film remains insulating with the three electrons of each Mn occupying the t_{2g} orbitals, thus leading to the GAF magnetic ordering. The local magnetic moments of each MnO_2 plane are shown in Table III, where it can be seen that the layer by layer magnetic moments coincide with the ones obtained in the $P=0$ regime. In the lower-left panel of Fig. 4 the character projected bandstructure onto the $\text{Mn}-e_g$ orbitals (red) and onto the O orbitals of the interfacial CMO layer (blue) are depicted, confirming the insulating behavior of the CMO film. From the lower-right panel of the same figure, it can be seen that the generated 2DHG comes from the interfacial oxygens of the BTO film, and it presents a non-spin-polarized $p_x + p_y$ character. As the magnetic order of this P regime corresponds to the G-AFM type, the total magnetic moment within each layer vanishes and, therefore, we plot only one spin projection of the bandstructure.

It is important to note that in the bandstructures of Figs. 3 and 4 there are other gray-colored bands that are crossing the Fermi level (not highlighted) which are spatially localized at the BTO-vacuum interface. This fact is obviously a consequence of the charge neutrality of the whole system.

To strengthen the robustness of our findings at the CMO/BTO interface we also analyze the electronic properties of a $(\text{CMO})_4/(\text{BTO})_{8.5}/(\text{CMO})_4$ trilayer, where the two nonzero polarization regimes can be simultaneously simulated [see Fig. 1(b)]. Taking into account our previous results, the CAF and the FM magnetic configurations of both the CMO1 and the CMO2 films are not considered. Therefore, we calculate only two different magnetic structures of the two films, obtaining the following four combinations: AAF-AAF, AAF-GAF, GAF-AAF, and GAF-GAF. As already mentioned in Sec. II, within this structural model, the CMO1/BTO interface represents the previous $P \uparrow$ regime while the BTO/CMO2 corresponds to the $P \downarrow$ one. It is straightforward to infer, from our total energy results presented in Table IV, that the ground state magnetic configuration is the AAF-GAF one, in agreement with the bilayer's results.

Further analysis can be obtained from the electronic properties of the system close to the Fermi level. In Fig. 5 we show the corresponding bandstructure highlighting the projection of the bands onto the d_{xy} orbitals of the Mn atoms of the CMO1 film (a) and onto the oxygen atoms located close to the BTO-CMO2 interface (b). From these two figures, the existence of the two dimensional electron and hole gases at the two interfaces is confirmed. In the case of negative carriers, this 2DEG is located at the CMO1-BTO interface that corresponds to the $P \uparrow$ regime and it is generated when the d_{xy} orbitals of the Mn atoms begin to be partially filled. It is important to note that the unit cell of the trilayer is rotated 45° with

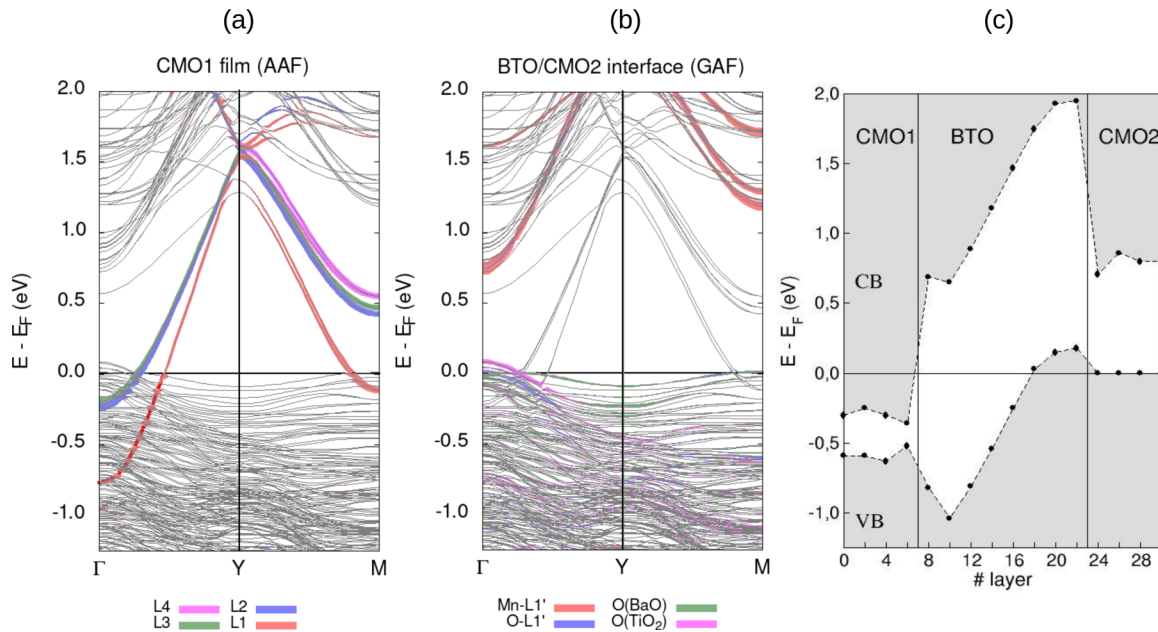


FIG. 5. Spin up + spin down bandstructure of the trilayer corresponding to its ground state AAF-GAF. (a) Projections onto the $\text{Mn}-d_{xy}$ orbitals for the different MnO_2 layers within the CMO1-film are highlighted [see Fig. 1(b)]. (b) Projections onto the $p_x + p_y$ orbitals of O atoms within both CMO2 and BTO interfacial layers. Mn- d orbitals are above 0.5 eV, as shown in the red-highlighted curve. (c) Calculated CB and VB profiles for the [001] direction of the trilayer. Note that layer No. 1 in this figure corresponds to layer named L4 in Fig. 1(b).

respect to the bilayer one and, therefore, the d_{xy} orbitals of the first correspond to the $d_{x^2-y^2}$ orbitals of the second system. At the BTO-CMO2 interface (P \downarrow regime) the charge carriers have positive character and come from the $p_x + p_y$ orbitals of the interfacial oxygen atoms that start to be partially empty. The effective mass of the 2DHG is isotropic and its value is $0.96m_e$, which is also of the same order as the ones reported for the 2DHG generated at the SrTiO₃/LaAlO₃ interfaces [15]. To summarize our results for the trilayer system, in Fig. 5(c) we show the band bending of the heterostructure. As it can be observed from this figure, where we plot both the top of the valence band and the bottom of the conduction band along the growth direction of the film, the 2DEG is spread within the whole CMO1 film, while the 2DHG is localized at the BTO side of the BTO/CMO2 interface.

IV. CONCLUSIONS

In this work we study, by means of *ab initio* calculations within the density functional theory, the electronic and magnetic properties of a CaMnO₃ ultrathin film grown on a strained BaTiO₃ ferroelectric film. We claim that this heterostructure presents a strong magnetoelectric interfacial coupling, characterized by a polarization driven magnetic transition from a G-type to an A-type antiferromagnetic configuration. Furthermore, coupled to this MEC we find a metallic behavior at the interface between these two insulators, where the charge character of the carriers can be tuned from electrons to holes by switching the electric polarization direction of the FE film. When this polarization points toward the CMO film, we find a spin-polarized 2DEG hosted by the Mn- $3d_{x^2-y^2}$ bands spatially localized within all the CMO layers, with a slight anisotropic dispersion around the Γ point with estimated effective masses of $0.48m_e$ and $0.37m_e$, for the

Γ -X and the Γ -M directions, respectively. On the other hand, when the FE polarization points away from the CMO interface, the charge carriers are of the hole type, and this 2DHG is non-spin-polarized with an O- $p_x + p_y$ character, spatially localized within the first interfacial BTO layer.

Summarizing, our results show that the magnetic ordering of the CMO and, consequently, the exchange interactions of the Mn atoms can be controlled by the ferroelectric polarization direction of BTO in this strained heterostructure. The polarization of FE film can be reversed using an external electric field, allowing us to manipulate the charge transfer at the interface and change the occupancy of the Mn e_g orbitals, thereby modifying the magnetic ordering of the ultrathin CMO film.

Overall, the proposed heterostructure offers unique potential opportunities to be considered as a fundamental part of future technological applications in spintronic devices. We hope that our findings stimulate further experimental studies toward miniaturization and interface engineering where the interfacial magnetoelectric coupling triggers and controls the physical properties.

ACKNOWLEDGMENTS

This work was partially supported by PICT-2016-0867 and PICT-2019-2128 of the ANPCyT, Argentina, and by H2020-MSCA-RISE-2016 SPICOLST Project No. 734187. We also acknowledge the financial support of European Commission through Marie Skłodowska-Curie Actions H2020 RISE with the projects MELON (Grant No. 872631) and ULTIMATE-I (Grant No. 101007825). Authors would like to acknowledge the access of equipment of “Servicio General de Apoyo a la Investigación (SAI), Universidad de Zaragoza.”

-
- [1] M. Fiebig, *J. Phys. D* **38**, R123 (2005).
 - [2] N. Spaldin and M. Fiebig, *Science* **309**, 391 (2005).
 - [3] W. Eerenstein, N. D. Mathur, and J. F. Scott, *Nature (London)* **442**, 759 (2006).
 - [4] P. Wadley, B. Howells, J. Železný, C. Andrews, V. Hills, R. P. Campion, V. Novák, K. Olejník, F. Maccherozzi, S. S. Dhesi *et al.*, *Science* **351**, 587 (2016).
 - [5] C. Zener, *Phys. Rev.* **82**, 403 (1951).
 - [6] P. G. de Gennes, *Phys. Rev.* **118**, 141 (1960).
 - [7] H. Kramers, *Physica* **1**, 182 (1934).
 - [8] J. B. Goodenough, *Phys. Rev.* **100**, 564 (1955).
 - [9] W. Meevasana, P. D. C. King, R. H. He, S.-K. Mo, M. Hashimoto, A. Tamai, P. Songsirithigul, F. Baumberger, and Z.-X. Sh, *Nat. Mater.* **10**, 114 (2011).
 - [10] A. Ohtomo and H. Hwang, *Nature (London)* **427**, 423 (2004).
 - [11] N. Reyren, S. Thiel, A. D. Caviglia, L. F. Kourkoutis, G. Hammerl, C. Richter, C. W. Schneider, T. Kopp, A.-S. Rüetschi, D. Jaccard *et al.*, *Science* **317**, 1196 (2007).
 - [12] A. Brinkman, M. Huijben, M. van Zalk, J. Huijben, U. Zeitler, J. C. Maan, W. G. van der Wiel, G. Rijnders, D. H. A. Blank, and H. Hilgenkamp, *Nat. Mater.* **6**, 493 (2007).
 - [13] M. Stengel, *Phys. Rev. Lett.* **106**, 136803 (2011).
 - [14] W. Niu, Y. Zhang, Y. Gan, D. V. Christensen, M. V. Soosten, E. J. Garcia-Suarez, A. Riisager, X. Wang, Y. Xu, R. Zhang *et al.*, *Nano Lett.* **17**, 6878 (2017).
 - [15] I. V. Maznichenko, S. Ostanin, A. Ernst, J. Henk, and I. Mertig, *Physica Status Solidi (b)* **257**, 1900540 (2020).
 - [16] V. Vildosola, F. Güller, and A. M. Llois, *Phys. Rev. Lett.* **110**, 206805 (2013).
 - [17] B. Meir, S. Gorol, T. Kopp, and G. Hammerl, *Phys. Rev. B* **96**, 100507(R) (2017).
 - [18] S. Di Napoli, C. Helman, A. M. Llois, and V. Vildosola, *Phys. Rev. B* **103**, 174509 (2021).
 - [19] V. Borisov, S. Ostanin, and I. Mertig, *Phys. Chem. Chem. Phys.* **17**, 12812 (2015).
 - [20] Y. Weng, W. Niu, X. Huang, M. An, and S. Dong, *Phys. Rev. B* **103**, 214101 (2021).
 - [21] W. Aggoune and C. Draxl, *npj Comput. Mater.* **7**, 174 (2021).
 - [22] L. Fang, W. Aggoune, W. Ren, and C. Draxl, *ACS Appl. Mater. Interfaces* **15**, 11314 (2023).
 - [23] B. Yin, P. Aguado-Puente, S. Qu, and E. Artacho, *Phys. Rev. B* **92**, 115406 (2015).
 - [24] A. L. Pedroso, M. A. Barral, M. E. Graf, A. M. Llois, M. H. Aguirre, L. B. Steren, and S. Di Napoli, *Phys. Rev. B* **102**, 085432 (2020).

- [25] C.-G. Duan, S. S. Jaswal, and E. Y. Tsymbal, *Phys. Rev. Lett.* **97**, 047201 (2006).
- [26] M. K. Niranjan, J. P. Velev, C.-G. Duan, S. S. Jaswal, and E. Y. Tsymbal, *Phys. Rev. B* **78**, 104405 (2008).
- [27] M. K. Niranjan, C.-G. Duan, S. S. Jaswal, and E. Y. Tsymbal, *Appl. Phys. Lett.* **96**, 222504 (2010).
- [28] J. D. Burton and E. Y. Tsymbal, *Phys. Rev. B* **80**, 174406 (2009).
- [29] S. Borek, I. V. Maznichenko, G. Fischer, W. Hergert, I. Mertig, A. Ernst, S. Ostanin, and A. Chassé, *Phys. Rev. B* **85**, 134432 (2012).
- [30] H. H. Wieder, *Phys. Rev.* **99**, 1161 (1955).
- [31] See Supplemental Material at <http://link.aps.org/supplemental/10.1103/PhysRevMaterials.8.034408> for the images of (1) epitaxial growth of BaTiO₃ thin film on an SrTiO₃ substrate, taken by high resolution scanning transmission electron microscopy with high angular annular dark field detector (HRSTEM-HAADF), (2) high-resolution synchrotron x-ray diffraction experiments on BTO/STO, and the piezoelectric response of BTO obtained by Piezoresponse Force Microscopy, which also contains Refs. [53–56].
- [32] P. E. Blöchl, *Phys. Rev. B* **50**, 17953 (1994).
- [33] G. Kresse and J. Furthmüller, *Phys. Rev. B* **54**, 11169 (1996).
- [34] G. Kresse and D. Joubert, *Phys. Rev. B* **59**, 1758 (1999).
- [35] J. P. Perdew and A. Zunger, *Phys. Rev. B* **23**, 5048 (1981).
- [36] D. Ceperley and B. Alder, *Phys. Rev. Lett.* **45**, 566 (1980).
- [37] A. Filippetti and W. E. Pickett, *Phys. Rev. Lett.* **83**, 4184 (1999).
- [38] A. Filippetti and W. E. Pickett, *Phys. Rev. B* **62**, 11571 (2000).
- [39] S. Keshavarz, Y. O. Kvashnin, D. C. M. Rodrigues, M. Pereiro, I. Di Marco, C. Autieri, L. Nordström, I. V. Solov'ev, B. Sanyal, and O. Eriksson, *Phys. Rev. B* **95**, 115120 (2017).
- [40] J. Neaton, C.-L. Hsueh, and K. Rabe, *Mat. Res. Soc. Symp. Proc.* **718**, D10.26 (2002).
- [41] J. B. Neaton and K. M. Rabe, *Appl. Phys. Lett.* **82**, 1586 (2003).
- [42] Y. Zhang, J. Sun, J. P. Perdew, and X. Wu, *Phys. Rev. B* **96**, 035143 (2017).
- [43] A. I. Liechtenstein, V. I. Anisimov, and J. Zaanen, *Phys. Rev. B* **52**, R5467 (1995).
- [44] N. N. Loshkareva, L. V. Nomerovannaya, E. V. Mostovshchikova, A. A. Makhnev, Y. P. Sukhorukov, N. I. Solin, T. I. Arbuzova, S. V. Naumov, N. V. Kostromitina, A. M. Balbashov *et al.*, *Phys. Rev. B* **70**, 224406 (2004).
- [45] D. A. Tenne, A. Bruchhausen, N. D. Lanzillotti-Kimura, A. Fainstein, R. S. Katiyar, A. Cantarero, A. Soukiassian, V. Vaithyanathan, J. H. Haeni, W. Tian *et al.*, *Science* **313**, 1614 (2006).
- [46] G. Gerra, A. K. Tagantsev, N. Setter, and K. Parlinski, *Phys. Rev. Lett.* **96**, 107603 (2006).
- [47] M. Fechner, S. Ostanin, and I. Mertig, *Phys. Rev. B* **77**, 094112 (2008).
- [48] R. D. King-Smith and D. Vanderbilt, *Phys. Rev. B* **47**, 1651 (1993).
- [49] K. Momma and F. Izumi, *J. Appl. Crystallogr.* **41**, 653 (2008).
- [50] E. Bousquet and N. Spaldin, *Phys. Rev. Lett.* **107**, 197603 (2011).
- [51] L. Vistoli, W. Wang, A. Sander, Q. Zhu, B. Casals, R. Cichelero, A. Barthélémy, S. Fusil, G. Herranz, S. Valencia *et al.*, *Nat. Phys.* **15**, 67 (2019).
- [52] G. H. Kwei, A. C. Lawson, S. J. L. Billinge, and S. W. Cheong, *J. Phys. Chem.* **97**, 2368 (1993).
- [53] S. V. Kalinin and A. Gruverman, *Scanning Probe Microscopy: Electrical and Electromechanical Phenomena at the Nanoscale* (Springer Science & Business Media, 2007), Vol. 1, pp. 171–214.
- [54] D. Kim, M. D. Rossell, M. Campanini, R. Erni, J. Puigmartí-Luis, X.-Z. Chen, and S. Pané, *Appl. Phys. Lett.* **119**, 012901 (2021).
- [55] K. J. Choi, M. Biegalski, Y. Li, A. Sharan, J. Schubert, R. Uecker, P. Reiche, Y. Chen, X. Pan, V. Gopalan *et al.*, *Science* **306**, 1005 (2004).
- [56] L. Shebanov, *Physica Status Solidi (a)* **65**, 321 (1981).